Analyst

ROYAL SOCIETY OF CHEMISTRY

PAPER

View Article Online
View Journal | View Issue

Check for updates

Cite this: *Analyst*, 2022, **147**, 4536

# High-recovery sorting of cancer cells from whole blood *via* periodic-focusing inertial microchip†

Xiao Li, Yijia Yang, Sarah C. Villareal, Kitiara Griffin and Dimitri Pappas *

Inertial microfluidic devices continue to show promise for label-free separation of cells from liquid biopsies and other biological samples. Serpentine-channel microfluidic devices capitalizing on inertial forces such as Dean flow have been demonstrated for cell separation, but are limited in performance due to the magnitude of the inertial lift and drag force gradients across the separation channel. We have developed a new flow design that uses periodic channel contractions to enhance the magnitude of the force gradient. Separation recover was 97% with the final sorter output consisting of 78% target cells. Separation efficiency was 87% for whole blood, which could be increased to 97% if the sample was diluted prior to sorting. The enrichment of cancer cells was over 1000-fold, and sorted cancer cells maintained a viability of 93.8% for 96 hours after sorting. In the analysis of blood plasma, breast cancer cells from a clinical patient were enriched 20×. The incorporation of periodic channel contractions in a Dean flow circuit resulted in an increase in Dean flow gradient according to simulation, resulting in sorting of small-diameter cancer cells in blood samples.

Received 8th August 2022,
Accepted 17th August 2022

DOI: 10.1039/d2an01310j

rsc.li/analyst

Published on 08 September 2022. Downloaded on 1/27/2026 6:45:06 AM.

## Introduction

High-throughput, high-efficiency manipulation of target cells/particles from biofluids has a potentially wide range of application in clinical diagnosis and various biochemical analysis.[1–3] The isolation and enrichment of a target cell phenotype in a diverse biological sample has implications in cancer,[4–7] sepsis,[8–12] asthma,[13] AIDS,[14–17] stroke,[18] and so on. Cell sorting in microfluidic systems can rely on affinity methods for specificity,[19–22] but can also be achieved using label-free methods that harness phenotypic differences such as density, cell size, deformability, and other factors.[23–29] The benefit of label-free approaches include assay speed, eliminating the need for a specific biomarker, and potentially lower cost.

Label-free cell sorting that leverages differential forces are particularly attractive when high-throughput separation is desired. Label-free methods can use an external force field, such as optical, acoustic, or magnetic gradients.[30] Other gradient fields include active centrifugal devices[31–36] and passive inertial devices. In the latter, the design of the flow circuitry itself gives rise to force gradients that facilitate label-free cell separation. Even though particle control flexibility and focusing accuracy are enhanced by introducing an external force field, the cost, control difficulty and fabrication complexity of peripheral control devices are also greatly increased.[37] In addition, external focusing methods require overcoming hydrodynamic particle drag, limiting their use in large sample volume applications.

In contrast, passive microfluidic techniques can manipulate particles by using channel structures[29,38,39] or intrinsic hydrodynamic forces,[5,28,40–42] and can operate at high flow rates. An increased flow rate is critical for processing sufficient sample volumes for lower concentration target cells. Inertial microfluidics are well suited to this task, and several designs have been developed to provide high sample volume analysis.[43–45] Channel geometry in inertial force focusing microfluidic sorters is one of the most important parameters that impact secondary flow and device performance.[46–48] Among all different channel geometries, the spiral channel has already been developed and applied to several biomedical applications.[3,49,50]

Sinusoidal channels have been introduced for the isolation of cells *via* inertial sorting.[51,52] The separation of particles based on size is governed by inertial lift forces trapping larger particles in the center of the flow stream, while smaller particles migrate to the sides of the channel due to secondary drag forces. The gradient of these forces contributes to the size resolution of inertial sorters and therefore the device performance for cell separation. The key innovation of our new design (Fig. 1) is the introduction of periodic contractions in the sinusoidal channels. These periodic contractions increase differences between lift and drag forces, more effectively trapping target cells while removing smaller blood cells. Lu *et al.* and Cha *et al.* first reported periodic contraction

*Department of Chemistry and Biochemistry, Texas Tech University, Lubbock, TX, 79409, USA. E-mail: d.pappas@ttu.edu; Fax: +806-742-1289; Tel: +806-834-1103*

†Electronic supplementary information (ESI) available: Blood lysing protocol (Section S1); flow cytometry analysis (Section S2); chip parameters (Table S1); fluent meshed images (Fig. S1); schematic illustration for separating rare tumor cells from whole blood (Fig. S2); flow rate optimization (Fig. S3); cell viability control (Fig. S4). Representative videos of particles and cells separation process (Videos S1–S5). See DOI: https://doi.org/10.1039/d2an01310j



This journal is © The Royal Society of Chemistry 2022

Published on 08 September 2022. Downloaded on 1/27/2026 6:45:06 AM.

structures to improve inertial sorting.[51,53] We have modified this approach to isolate small-diameter cancer cells (A549 lung cancer cells) from blood samples and breast cancer cells from blood plasma. We report an improvement in cell recovery and separation enrichment when compared to extant approaches. Recovery of A549 cells from blood was 85.6% in whole blood, or 97.4% when the sample was diluted prior to analysis. With a 1000-fold recovery ratio, this new design has the potential for high-recovery sorting for smaller-diameter cancer cells.

## Theory

In a microfluidic channel of the length scales used in this work, particle lateral displacement in flow is governed by wall-induced lift forces and shear-gradient-induced lift forces.[54] Wall-induced lift forces ($F_{WL}$) and shear-gradient-induced lift forces ($F_{SG}$) are expressed as

$$F_{WL} = \frac{f_{WL}\rho {U_m}^2 {a_p}^6}{{D_h}^4}, \quad (1)$$

and

$$F_{SG} = \frac{f_{SG}\rho {U_m}^2 {a_p}^4}{{D_h}^2}. \quad (2)$$

where $f_{WL}$ and $f_{SG}$ are lift coefficients, $\rho$, $a_p$, and $U_m$ refer to the density of fluid, cell/particle diameter, and the maximum fluid velocity, respectively.[44] $D_h$ which is the hydraulic diameter of the channel is defined as $D_h = 2wh/(w + h)$, where $w$ and $h$ are channel width and height respectively.[5] In straight channel, the equilibrium positions of different particles will be determined by the balance between these two lift forces.[55]

In curved semicircle channel, a secondary flow generated by the viscous fluid velocity difference between the edge and the center of the channel is introduced to produce a stable Dean drag force ($F_D$) along the channel's cross-section and therefore impact the particle equilibrium positions. Microstructures or the periodic variation of the channel width can also cause secondary Dean flows effectively.[56] Dean flow force directions are perpendicular to the main flow whose strength are usually characterized by a dimensionless Dean number, $D_e$, which can be expressed as,[44]

$$D_e = \frac{\rho U_m D_h}{\mu}\sqrt{\frac{D_h}{2R}} = R_e\sqrt{\frac{D_h}{2R}} \quad (3)$$

where $\mu$ is the viscosity of the fluid, $R_e$ is the Reynolds number of the channel, and $R$ is the radius of the channel.[57] The magnitude of the Dean flow scales with ${U_m}^2$ as,[58]

$$U_D \sim {D_e}^2\frac{\mu}{\rho D_h} \quad (4)$$

Unlike straight channels, particle positions in curved channels are determined by the balance between $F_L$ and $F_D$. The Dean drag force is expressed as,[59]

$$F_D = 3\pi\mu a_p U_D \sim \frac{\rho {U_m}^2 {a_p}{D_h}^2}{R} \quad (5)$$

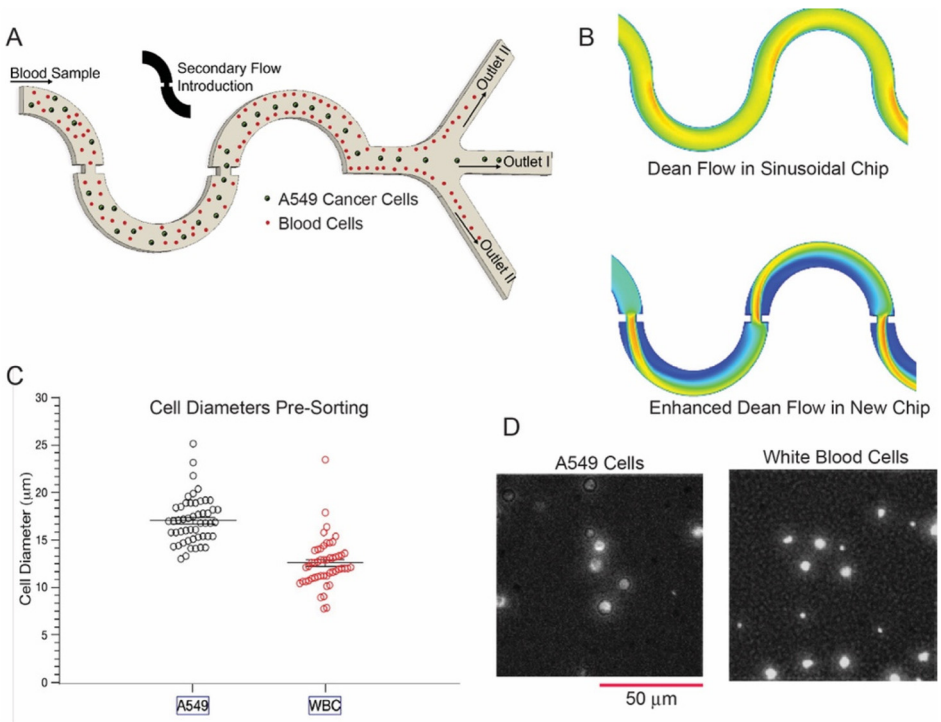


**Fig. 1** A new inertial cell sorter (A) incorporating periodic contractions that increase the differences between inertial and drag forces for improved inertial separation. Simulation (B) of the velocity profile in the channel, showing increased velocity gradients in the new design when compared with extant sinusoidal channels. The new design was used to isolate small-diameter A549 lung cancer cells spiked into blood (C and D). The small diameter cancer cell was able to be separated from whole blood.

Published on 08 September 2022. Downloaded on 1/27/2026 6:45:06 AM.

$R_f$ is another empirical parameter which represents the ratio of inertial lift force to Dean drag force,

$$R_f = \frac{2Ra_p{}^2}{D_h{}^3} \quad (6)$$

A too small value of $R_f$ would generate chaotic particle motion rather than deterministic particle focusing.[1] According to eqn (6), larger particles are more easily dominated by inertial lift force, while smaller particles more easily show a secondary flow drag force dominant behavior. If secondary flow drag force dominates, the equilibrium position of particles or cells potentially moves towards the inner channel side in the case of symmetric channel or towards the channel center in the case of the asymmetric channel. The outcome is reversed if the inertial lift force dominates.[5] Therefore for our sorter, we expect the repeating contraction structure can produce additional secondary flow at the entry and exit and the sudden contraction could give rise to stronger net inertial lift forces[51] to result that large cells/particles will remain near the center of the channel and small cells/particles will be directed to side walls. The contraction of the channel also changes the hydraulic diameter, modulating the magnitude of Dean flow. We hypothesized that this periodic contraction and increase in Dean flow would sharpen flow streams, providing improved flow gradients perpendicular to the main, driven fluid flow.

## Materials and methods

### Chip design and fabrication

The inertial focusing microfluidic design and the distribution of different cells in each outlet is illustrated in Fig. 1. The main sorting channel had a width of 240 μm, the entire chip had a channel height of 50 μm. Each turn of the flow channel had a radius of 500 μm. The contractions were introduced after each half turn, constricting the flow channel from 240 μm to 100 μm for a length of 70 μm before restoring channel width. The contraction section (Fig. 1) was repeated 20 times to form the final sorting channel. The device includes one inlet for sample input, two outlets to collect small cells/particles from two sidewall regions (outlet II) and large cells/particles from the central channel (outlet I), respectively. All microdevices were fabricated with standard photolithography and polydimethylsiloxane (PDMS) soft lithography techniques.[60,61]

### Cell culture

The A549 small-cell lung cancer cell line was purchased from the American Type Culture Collection (ATCC. Cells were cultured in RPMI 1640 medium (Hyclone) supplemented with 1% penicillin–streptomycin stabilized solution (Sigma-Aldrich) and 10% fetal bovine serum (Hyclone). All cell flasks were stored at 37 °C containing 5% (v/v) $CO_2$ and were sub-cultured every 4 days. 0.25% trypsin–EDTA solution (Thermo Fisher Scientific) were utilized to detach adherent cancer cells from the flask prior to each experiment.

### Fluorescent polystyrene microsphere sample preparation

4 and 13 μm dye-doped polystyrene microspheres were uses for initial device development (Thermo Fisher Scientific). Particle mixtures were suspended in phosphate buffered saline (PBS) buffer at a concentration of ~$3.6 \times 10^6$ particles per mL.

### Blood sample preparation

Commercially obtained, deidentified peripheral blood samples (Becton-Dickinson) were purchased and stored in the refrigerator at 4 °C until use. Whole blood samples were diluted approximately 100 times prior to each cell experiments and the typical blood cell concentration was ~$4 \times 10^7$ counts per mL.

### Blood plasma analysis

In order to demonstrate the use of this sorter chip with a clinically relevant sample, we used plasma from a commercial biobank. Samples were obtained from Precision for Medicine, and were stored, analyzed, and treated in accordance with the guidelines set by the Texas Tech University Institutional Review Board for human subjects research. Informed consent was obtained from the commercial source (Precision for medicine). The patient was a 49-year-old, white, non-Hispanic with stage II breast cancer. The sample was deidentified and arrived as frozen EDTA-treated plasma.

### Fluorescence staining

For characterization experiments (cell viability tests experiments were not included), cancer cells were stained with Mito Tracker Green (Thermo Fisher Scientific) and white blood cells were stained with propidium iodide (PI, invitrogen) for visualization and quantitation prior to mixing.[61]

### Cell viability assay

A549 cells spiked in blood were processed through the microfluidic sorter and isolated A549 cells were cultured after separation in Petri dishes with RPMI 1640 medium for 12, 36, 72 and 96 h and stained *via* propidium iodide (PI) and Hoechst 33342 (Invitrogen) to assess the influence of fluid pressure and shear stress.

### Experimental setup

Each individual experiment was processed with a new chip to avoid cross-contamination by residual cells/particles and were primed with PBS buffer to remove bubbles and reduce the adhesion between cells/particles and channel structures. All aqueous samples were loaded into 5 mL syringes and were injected by syringe pumps (KD Scientific, USA). The outlet orifices were connected to two centrifuge vials *via* PTFE tubing to collect samples and tubing length was the same to equalize channel pressure. Microdevices were observed under a fluorescence microscope (Olympus) to acquire visual cell/particle trajectories. All captured images and videos were subsequently

 This journal is © The Royal Society of Chemistry 2022

Published on 08 September 2022. Downloaded on 1/27/2026 6:45:06 AM.

processed using ImageJ software (National Institutes of Health).

### Statistical analysis

Each experiment was performed in triplicate. Data are presented as mean values ± SEM (standard error of mean). All statistical analysis was performed at $p < 0.05$ level of significance.

### Simulations

ANSYS Fluent 2021 R1 software was utilized to quantitatively simulate the velocity distribution to guide the experimental setup. To verify the enhanced effect of contraction on the secondary flow, we compared the velocity distribution in the designed microfluidic chip and normal sinusoidal chips.

## Results and discussion

### Simulation of velocity distribution in designed microfluidic chips

All the simulations were conducted at a flow rate of 435 μL $min^{-1}$ ($R_e$ = 50) which is consistent with that used in the experiments. The Fluent model consists of sinusoidal channel with the same geometric dimensions as the experiments. The boundaries other than the inlet and the outlet were set as a non-slip condition. We were particularly interested in the flow field among three cross-sections (A–C as defined in Fig. 2). Fig. 2b demonstrates the representative velocity distribution along one of chip loops, in which all left sides are inner sides and all right sides are outer sides. The results indicated that the velocity gradient in the chip with expansions was greater

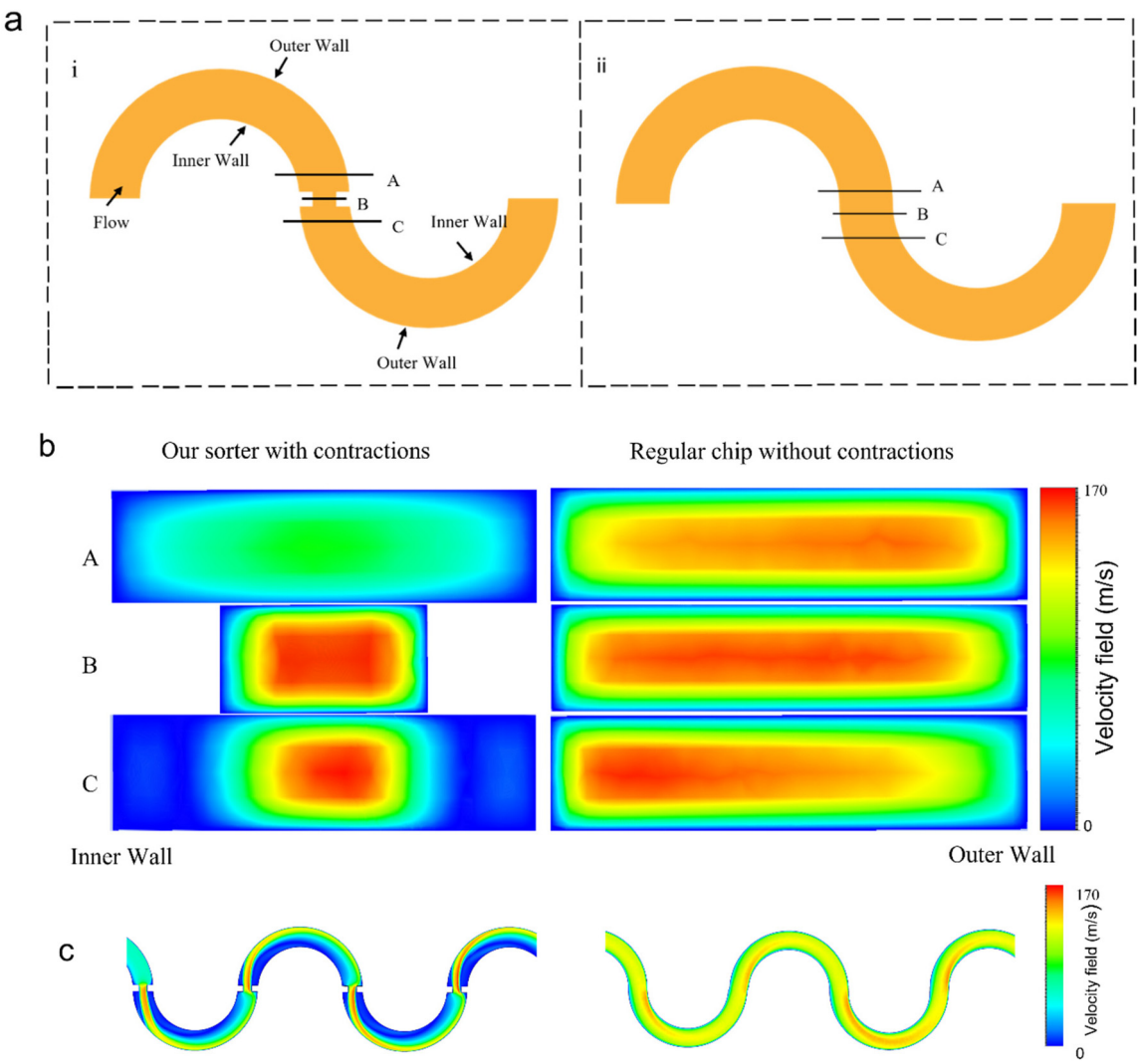


**Fig. 2** Numerical simulation of the velocity magnitude map at different three cross-sections. (a) Three cross-sections (A–C) were selected to visualize the velocity magnitude along our new microdevice (i) and a normal sinusoidal microchip (ii). (b) Simulated flow field along the representative three cross-sections (A–C). All the right sides denote the outer wall of the channel. The contraction focuses the flow, increasing the Dean flow due to the decrease in hydraulic radius. (c) Comparison of the velocity distribution in the new sorter compared to an unmodified channel. Each contraction structure focuses flow velocity, resulting in a higher gradiate of Dean flow across the channel (perpendicular to the driven flow axis).

Published on 08 September 2022. Downloaded on 1/27/2026 6:45:06 AM.

than that in the regular sinusoidal channel (as shown in Fig. 2c). This is expected due to the contraction of the hydraulic radius and subsequent increase in Dean flow. Compared with normal sinusoidal channel where Dean flow at cross-section A–C show similar velocity profile, an enhanced velocity gradient could be generated when the fluid flow through the contractions.

### Flow rate optimization

Different width of contractions ($W$ = 160, 140, 120, and 100 μm) were formed on the base channel and polystyrene beads (~$3.6 \times 10^6$ particles per mL) were prepared and injected inside our sorter at 435 μL $min^{-1}$ ($R_e$ = 50). Fig. 3 shows two differently sized particle distributions at representative locations. All particles showed similar trajectories, which is spreading randomly upstream but exhibiting a focusing effect started from the midstream and flowing strictly to the corresponding outlet in the end. As shown in the Fig. 3 with each contraction, the equilibrium positions of small particles move closer to the sidewall of the channel and focus as a line flowing through outlet II, and large particles move closer to the centerline flowing through outlet I. It is notable that 4 μm particles formed two clear streaks near the sidewall of the channel for 120 and 100 μm contraction structure and a small fraction of

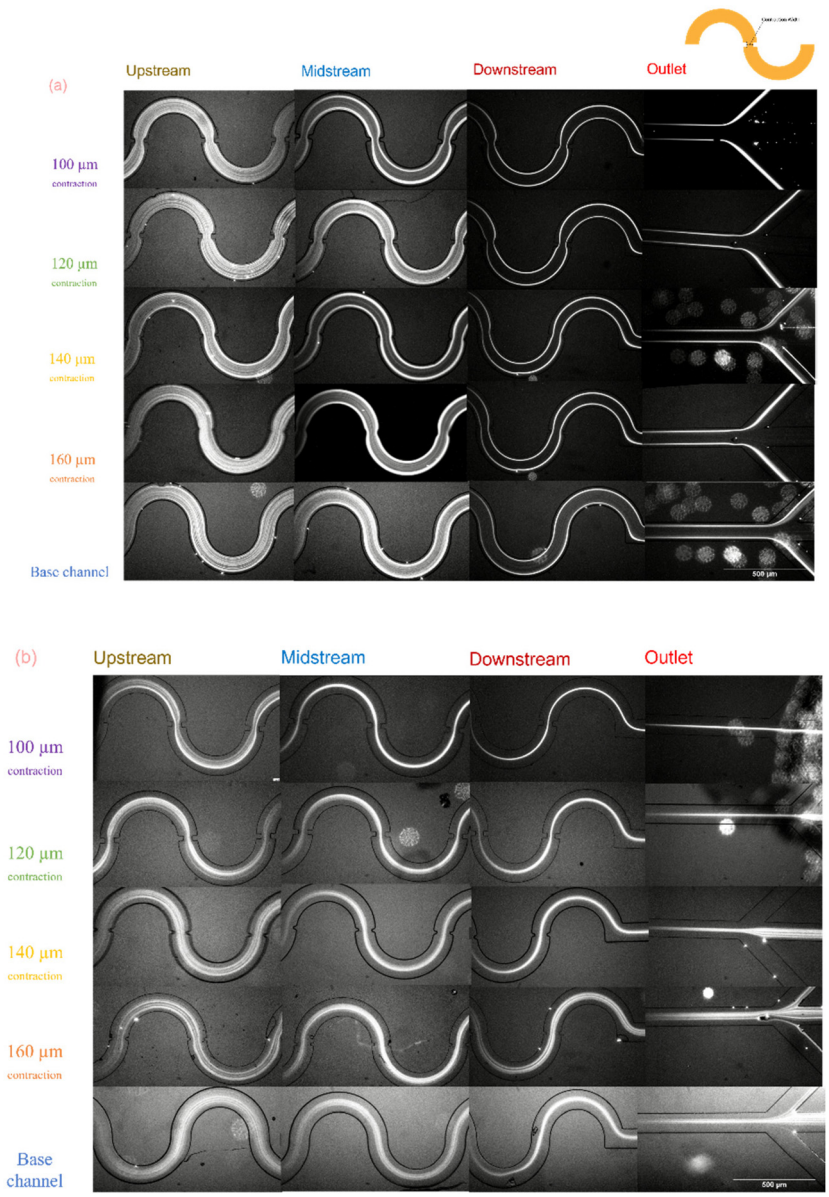


**Fig. 3** Fluorescence microscopic images of 4 and 13 μm particles undergoing inertial focusing in 5 different channel designs with various contractions at different positions (upstream, midstream, downstream and outlet) of the sorter at 435 μL $min^{-1}$ ($R_e$ = 50). (a) Fluorescence images of 4 μm particles at representative positions. (b) Fluorescence images of 13 μm particles at different positions. Scale bar is 500 μm. Diameter-based focusing is clearly observed.


This journal is © The Royal Society of Chemistry 2022

Published on 08 September 2022. Downloaded on 1/27/2026 6:45:06 AM.

residual particles were not able to be focused using 160, 140 μm contractions and base curved channels. No obvious focusing differences but a relatively thinner streak was observed for 13 μm particles using narrower contraction structure. Experimental results demonstrated and proved that narrower contractions can introduce a more pronounced secondary flow as expected. Therefore, sorters with 100 μm contractions were chosen for subsequent particle and cell separation studies.

Flow rate optimization was also studied using 4 and 13 μm polystyrene beads and a figure of particle focusing using flow rate (435 μL $min^{-1}$ ($R_e$ = 50), 522 μL $min^{-1}$ ($R_e$ = 60) and 609 μL $min^{-1}$ ($R_e$ = 70)) was provided in ESI (ESI Fig. S3†). Two sized polystyrene beads exhibited identical trajectories with two particle trajectories shown in Fig. 3 over the entire velocity range. 4 μm particles focusing on two streaks and exit from the two side channel and 13 μm particles focusing on centerline and exit from the middle outlet. Under the microscope, this behavior was not affected by the velocity but was only determined by the interaction between the contraction-induced Dean drag force and lift force. When the flow rate was higher than 698 μL $min^{-1}$ ($R_e$ = 80), the back pressure resulted in some of the chips leaking. Therefore, considering the throughput cancer cells can stand and chip leaking, the flow rate was set up to 609 μL $min^{-1}$ ($R_e$ = 70) for achieving good separation efficiency and high throughput without leakage.

### Characterization of polystyrene particles separation performance

We then applied 4 and 13 μm PS particles to characterize the separation effectiveness of our sorter. Samples were prepared following the procedure described in Experimental section and injected into sorters at the optimized 609 μL $min^{-1}$ flow rate (ESI Videos 1 and 2†). The recovery ratio and purity of the particles collected from each outlet were calculated to quantitatively evaluate the performance and defined as,

$$\text{Recovery ratio} = \frac{\text{Number of target particles in each outlet}}{\text{Number of target particles in all outlet}} \quad (7)$$

$$\text{Purity} = \frac{\text{Number of target particles in each output}}{\text{Total number of particles in each output}} \quad (8)$$

Collected particle were also characterized by flow cytometry and data is shown in Fig. 4a. After a single sorting pass, 96.8% of 13 μm particles can be recovered and 92.0% of 4 μm particles were removed. Fig. 3b demonstrates the fluorescence microscopy images of collected samples from inlet, outlet I and outlet II. After conducting three parallel experiments, over 96.5% of the particles collected from middle outlet (outlet I) are 13 μm particles, while over 92.2% of the particles in the outside outlet (outlet II) are 4 μm particles. A small number of particles will exit from outlet I and cannot be focused due to the inevitable particle–particle collision in microscale channels. Cascade chips would be needed to achieve simultaneous separation of multiple particles in future chip designs.

### Characterization of cell separation performance

We next characterize the cell separation performance of our sorter by spiking ~$10^6$ counts per mL (~2.0% of all cell numbers) A549 cancer cells (cell diameters and distributions were measured and summarized in ESI Table S1†) into diluted blood samples ($4 \times 10^7$ counts per mL). All blood samples were 2 mL prepared following the description in the Experimental section and pumped through the sorter at 609 μL $min^{-1}$. Other than spiked cancer cells, the rest of the cell populations in the cell sample were mainly red blood cells (~6–8 μm), white blood cells (~10–15 μm).[62] As the average size of blood cells are smaller than the cancer cells, so cancer cells can be theoretically focused at the central channel whereas blood cells can be focused near the sidewall on the basis of differential focusing principle along the channel's cross-section.

The bright-field images illustrated in Fig. 5a and b shows the cell trajectory at two different locations (midstream and trifurcated outlet) and a separation movie can be found in ESI Video 3.† At the start of the sorter, blood samples spiked with A549 cells distribute randomly along the channel's cross section. After passing through several repeating units, most of the tumor cells can be focused at the center of the channel which forms the visualized middle streak, and the majority of red blood cells in addition to the relatively lower amount of WBCs can be focused near the wall and flow towards the side wall, forming the two side streaks. A significant amount of space (~50 μm) were observed between the trajectory of middle streak and two sidewall streaks. As shown in Fig. 5b, smaller blood cells and larger A549 cells will be directed into the correcting outlets after the complete inertial focusing. Fig. 5c and e illustrate the photograph and microscopic images of the original cell mixture and collected samples from two outlets. Input cell mixture contained stained cancer cells at a preset ratio around 2% with reference to all cells. Large amount of red blood cells exiting from outlet II lead to the collected sample appearance qualitatively matching the input sample. From Fig. 5e, high ratio of tumor cells can be easily obtained using our sorter, which could be coupled to next generation bioinformatic analysis.

Separation efficiency and purity were calculated to quantitatively assess the sorter performance. Fig. 5d illustrates the percentage of both tumor cells and blood cells in inlet and outlets, the percentage in each outlet can be regarded as the recovery ratio of specific cells and the blood cell percentage in outlet II can stand for the sorter removing ratio of blood cells as well. After a single sorting process, 86.7% of A549 cells could be recovered compared with the original input sample. Due to the unavoidable cell–cell collision at high cell concentration, a small portion of blood cells were also collected from outlet I, as indicted by the recovery ratio of 13.7% in outlet I. The average purity of isolated A549 cells from outlet I were measured and can reach 28.3%, representing over 14-fold purity enrichment.

High-reliability is also another feature of our sorter other than high-recovery ratio. After the inertial sorting process, no

Published on 08 September 2022. Downloaded on 1/27/2026 6:45:06 AM.

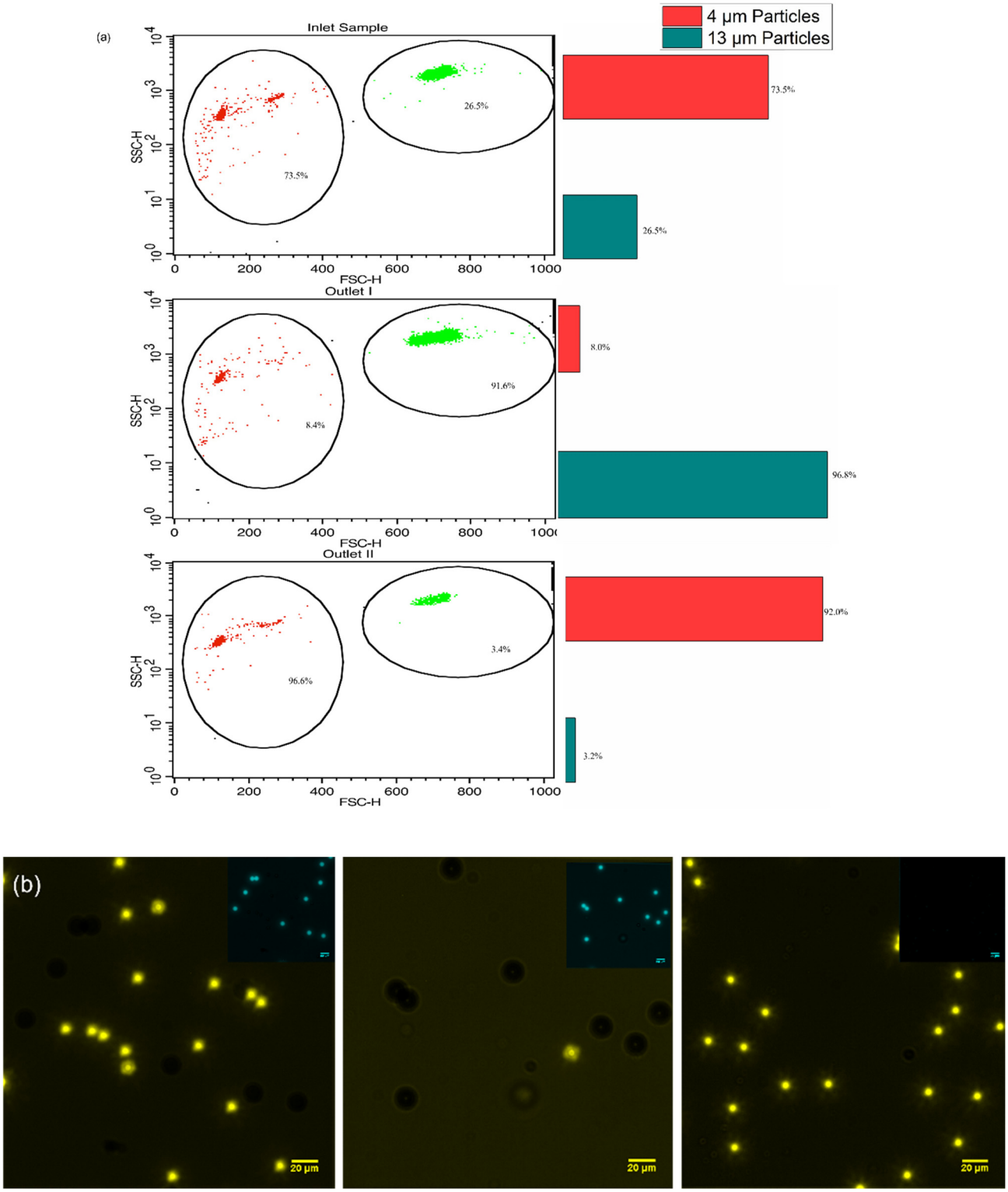


**Fig. 4** (a) Flow cytometer scatter plots (forward *vs.* side scatter (FSC *vs.* SSC)) collected from inlet and two outlets with the corresponding bar graphs illustrated the particle proportions at the optimized 609 μL $min^{-1}$ flow rate. 4 μm particles occupied 73.5% of all particle numbers and 26.5% of particles are 13 μm particles in inlet mixture. After a single sorting, 96.8% of 13 μm particles could be recovered from outlet I with 8.0% 4 μm particles while 92.0% of 4 μm particles were removed from outlet II with 3.2% of 13 μm particles. (b) Microscopic images of 4 μm particles sampled from inlet, outlet I and outlet II (top-right corner images are fluorescence images of 13 μm particles). Scale bar is 20 μm.


This journal is © The Royal Society of Chemistry 2022

Published on 08 September 2022. Downloaded on 1/27/2026 6:45:06 AM.

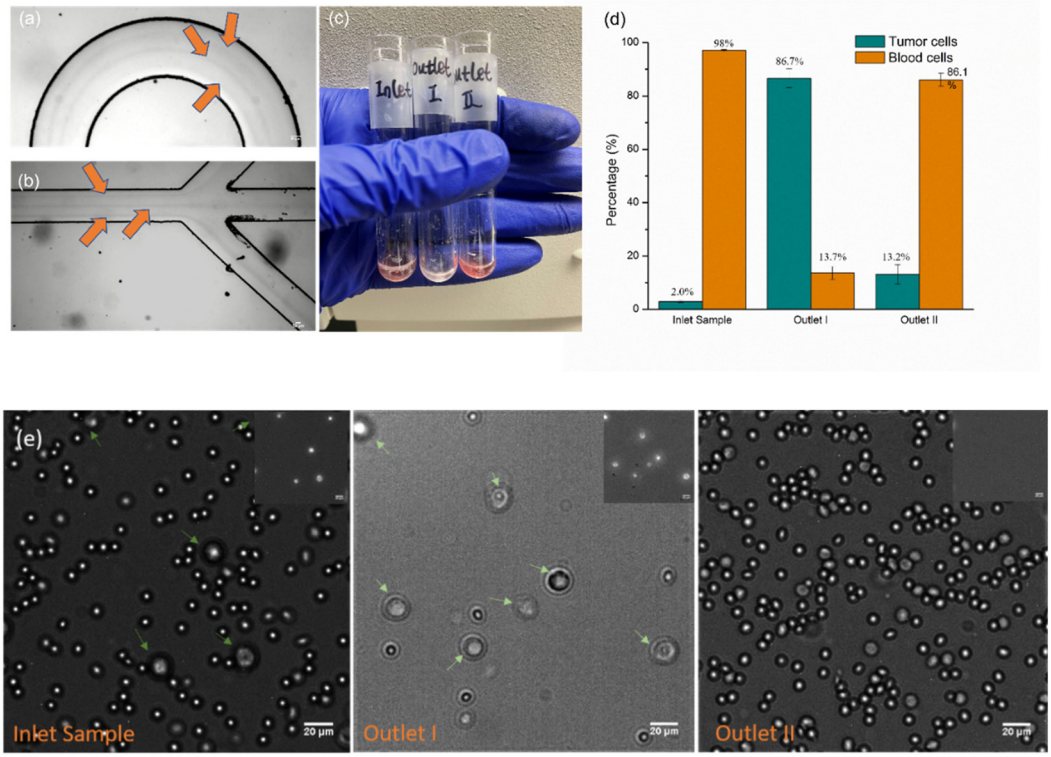


**Fig. 5** Separation of A549 lung cancer cells using inertial sorting devices with 100 μm contractions. (a and b) Bright field images of three trajectory streaks at the downstream and trifurcated outlet for A549 cell separation. Red blood cells and most leukocytes (having size difference with tumor cells) were collected in outlet II while cancer cells and a small fraction of leukocyte were collected in outlet I. The flow rate was 609 μL $min^{-1}$ ($R_e$ = 70). Scale bar is 50 μm. (c) Photograph of the samples collected from inlet, outlet I and outlet II. (d) Percentage of tumor cells and blood cells in inlet and each outlet. (e) Microscopic images of the samples collected from inlet, outlet I and outlet II. Fluorescence images of stained tumor cells under fluorescence were inset at the top-right corners of each image for visualization. Scale bar is 20 μm.

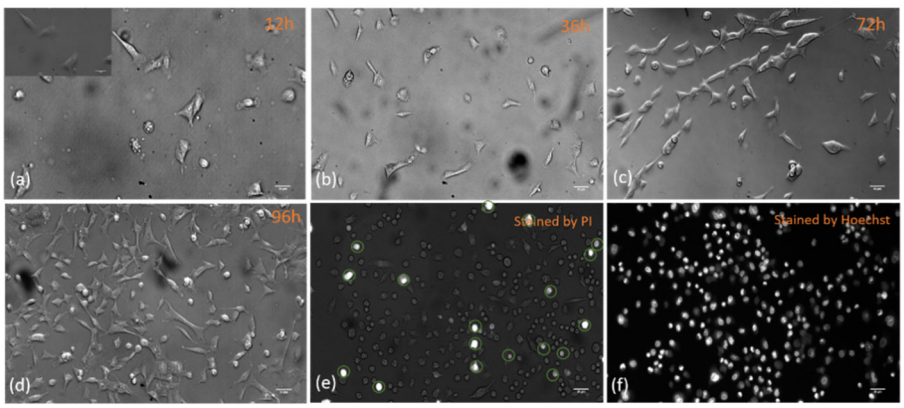


**Fig. 6** (a–d) Microscopic images of the re-cultured tumor cells 12, 36, 72 and 96 h. Scale bar is 50 μm. (e) 96 h cultured A549 cells were stained with PI and fluorescence cells are dead cells and were circled. (f) 96 h cultured A549 cells were stained with Hoechst for comparison purpose with graph e (same position with picture taken for graph (e)).

clogging or leaking was observed even processing the sample with this high concentration and high flow rate, demonstrating the potential of this sorter to be employed for size-based and label-free separation of various adherent cancer cells in clinics.

## Cell viability test

Intact, viable cancer cells are required for further downstream analysis. Therefore, cell viability tests were conducted to evaluate the effects of high fluidic pressure, cell interactions, and

Published on 08 September 2022. Downloaded on 1/27/2026 6:45:06 AM.

Table 1 Analysis of clinical plasma samples

| Analysis (hemacytometer) | EpCAM + in plasma | EpCAM + in separated plasma | CD71 + in separated plasma |
|---|---|---|---|
| 1 | 1 | 2 | 2 |
| 2 | 0 | 0 | 0 |
| 3 | 0 | 0 | 4 |
| 4 | 0 | 0 | 0 |
| Total cells per μL | 10 | 20 | 60 |

Note: CD71+ cells were not detected in the whole, unprocessed blood plasma.

shear stress. 2 mL cell samples were prepared without any fluorescent staining and pumped into the device. The target cancer cells were then harvested from outlet I and re-cultured for 12, 36, 72, and 96 h. Microscopic images of the re-cultured cells are shown in Fig. 6 at different time scales. The cell morphologies and viabilities were consistent with the A549 cells cultured in the original flasks, demonstrating that the sorter presented in this work has a negligible influence on cancer cell functionalization and collected cells can be re-cultured according to following generation research. The 96 h cultured cells were also characterized by PI and Hoechst. As shown in Fig. 6e, 93.8% of the cells maintained the desired proliferation capacity and viability after separation while normal cultured cancer cells (which were used as control, ESI Fig. S4†) can maintain 94.2% cell viability after cultured 96 h under the same condition.

### Isolation of cancer cells from patient blood plasma

Blood plasma from a breast cancer patient is shown in Table 1. The blood plasma was diluted 10× in phosphate buffered saline to reduce sample viscosity but was otherwise unaltered. Samples before and after separation were stained with fluorescent antibodies for EpCAM or CD71 and measured *via* a hemacytomer.[21,63,64] The fluid collected in Outlet 1 was stained and tested in an identical manner. The number of cells observed is consistent with the low cell concentration and the small volumes measured *via* hemacytometer. As seen in the pre-separation, the label-free separation showed a 20× enrichment, when factoring in dilution. While a preliminary step, this shows our chip utility for the analysis of clinical samples.

## Conclusion

In this work, we present a totally passive inertial microfluidic cell sorting device with a base serpentine channel and integrated periodic contraction with repeating units to realize efficient, stable, high-throughput, and label-free tumor cell separation using a relatively small-diameter adherent cancer cell line (A549 lung cancer cell line). We first verified the conceptual design, and then we characterized the chip performance with polystyrene particles and high concentration cells. Characterization results show that over 96.5% and 92.2% of 13 μm particles and 4 μm particles can be recovered respectively and greater than 86.7% recovery ratio is achieved with a target cell purity of 28.3% which is relatively low but acceptable and inescapable due to the unavoidable cell–cell collision especially at this high-flow rate. All cells were recovered with excellent viabilities and can be re-cultured for different kinds of biomedical research and downstream disease diagnosis. Then, our sorter was applied to separate rare tumor cells from whole blood with over 91.3% blood cell removal and 85.6% average tumor cell recovery ratio. Over $10^3$ enrichment factor by spiking 1000 tumor cells in 1 mL diluted whole blood was realized. Finally, to investigate the influence of WBCs, we demonstrated the sorter is able to separate rare tumor cells from relatively high concentration WBCs at a good performance with 97.4% recovery ratio.

## Conflicts of interest

There are no conflicts to declare.

## Acknowledgements

This work was supported by a grant from the Cancer Research and Prevention Institute of Texas (CPRIT RP180862).

## References

1 Y. Zhou, Z. Ma and Y. Ai, *Microsyst. Nanoeng.*, 2018, **4**, 1–14.
2 Y. Liu, D. Ren, X. Ling, W. Liang, J. Li, Z. You, Y. Yalikun and Y. Tanaka, *Sensors*, 2018, **18**, 3672.
3 P.-H. Tsou, P.-H. Chiang, Z.-T. Lin, H.-C. Yang, H.-L. Song and B.-R. Li, *Lab Chip*, 2020, **20**, 4007–4015.
4 A. Abdulla, W. Liu, A. Gholamipour-Shirazi, J. Sun and X. Ding, *Anal. Chem.*, 2018, **90**, 4397–4405.
5 A. Abdulla, T. Zhang, K. Z. Ahmad, S. Li, J. Lou and X. Ding, *Anal. Chem.*, 2020, **92**, 16170–16179.
6 F. Cui, J. Ji, J. Sun, J. Wang, H. Wang, Y. Zhang, H. Ding, Y. Lu, D. Xu and X. Sun, *Anal. Bioanal. Chem.*, 2019, **411**, 985–995.
7 A. Dalili, E. Samiei and M. Hoorfar, *Analyst*, 2019, **144**, 87–113.
8 U. Hassan, T. Ghonge, B. Reddy Jr., M. Patel, M. Rappleye, I. Taneja, A. Tanna, R. Healey, N. Manusry, Z. Price, T. Jensen, J. Berger, A. Hasnain, E. Flaugher, S. Liu, B. Davis, J. Kumar, K. White and R. Bashir, *Nat. Commun.*, 2017, **8**, 15949.
9 Y. Zhang, W. Li, Y. Zhou, A. Johnson, A. Venable, A. Hassan, J. Griswold and D. Pappas, *Analyst*, 2018, **143**, 241–249.
10 Y. Zhang, Y. Zhou, W. Li, V. Lyons, A. Johnson, A. Venable, J. Griswold and D. Pappas, *Anal. Chem.*, 2018, **90**, 7204–7211.

 This journal is © The Royal Society of Chemistry 2022

Published on 08 September 2022. Downloaded on 1/27/2026 6:45:06 AM.

11 Y. Zhang, Y. Zhou, Y. Yang and D. Pappas, *Analyst*, 2021, **146**, 2110–2125.
12 Y. Zhou, Y. Zhang, A. Johnson, A. Venable, J. Griswold and D. Pappas, *Anal. Chim. Acta*, 2019, **1062**, 110–117.
13 C. Murray, H. Miwa, M. Dhar, D. E. Park, E. Pao, J. Martinez, S. Kaanumale, E. Loghin, J. Graf, K. Rhaddassi, W. W. Kwok, D. Hafler, C. Puleo and D. Di Carlo, *Lab Chip*, 2018, **18**, 2396–2409.
14 X. Cheng, A. Gupta, C. Chen, R. G. Tompkins, W. Rodriguez and M. Toner, *Lab Chip*, 2009, **9**, 1357–1364.
15 X. Cheng, D. Irimia, M. Dixon, K. Sekine, U. Demirci, L. Zamir, R. G. Tompkins, W. Rodriguez and M. Toner, *Lab Chip*, 2007, **7**, 170–178.
16 W. Li, Y. Gao and D. Pappas, *Biomed. Microdevices*, 2015, **17**, 113.
17 N. N. Watkins, U. Hassan, G. Damhorst, H. Ni, A. Vaid, W. Rodriguez and R. Bashir, *Sci. Transl. Med.*, 2013, **5**, 214ra170.
18 S. R. Pullagurla, M. A. Witek, J. M. Jackson, M. A. Lindell, M. L. Hupert, I. V. Nesterova, A. E. Baird and S. A. Soper, *Anal. Chem.*, 2014, **86**, 4058–4065.
19 H. Chen, B. Cao, H. Chen, Y. S. Lin and J. Zhang, *Biomed. Microdevices*, 2017, **19**, 66.
20 W. Huang, C. L. Chang, N. D. Brault, O. Gur, Z. Wang, S. I. Jalal, P. S. Low, T. L. Ratliff, R. Pili and C. A. Savran, *Lab Chip*, 2017, **17**, 415–428.
21 W. Li, Y. Zhang, C. P. Reynolds and D. Pappas, *Anal. Chem.*, 2017, **89**, 7340–7347.
22 Y. Zhang, V. Lyons and D. Pappas, *Electrophoresis*, 2018, **39**, 732–741.
23 N. Nivedita, N. Garg, A. P. Lee and I. Papautsky, *Analyst*, 2017, **142**, 2558–2569.
24 N. Nivedita and I. Papautsky, *Biomicrofluidics*, 2013, **7**, 54101.
25 D. Robert, N. Pamme, H. Conjeaud, F. Gazeau, A. Iles and C. Wilhelm, *Lab Chip*, 2011, **11**, 1902–1910.
26 F. Shen, H. Hwang, Y. K. Hahn and J. K. Park, *Anal. Chem.*, 2012, **84**, 3075–3081.
27 A. Urbansky, F. Olm, S. Scheding, T. Laurell and A. Lenshof, *Lab Chip*, 2019, **19**, 1406–1416.
28 M. E. Warkiani, G. Guan, K. B. Luan, W. C. Lee, A. A. Bhagat, P. K. Chaudhuri, D. S. Tan, W. T. Lim, S. C. Lee, P. C. Chen, C. T. Lim and J. Han, *Lab Chip*, 2014, **14**, 128–137.
29 N. Xiang, J. Wang, Q. Li, Y. Han, D. Huang and Z. Ni, *Anal. Chem.*, 2019, **91**, 10328–10334.
30 P. Li, Z. Mao, Z. Peng, L. Zhou, Y. Chen, P. H. Huang, C. I. Truica, J. J. Drabick, W. S. El-Deiry, M. Dao, S. Suresh and T. J. Huang, *Proc. Natl. Acad. Sci. U. S. A.*, 2015, **112**, 4970–4975.
31 R. Burger, D. Kirby, M. Glynn, C. Nwankire, M. O'Sullivan, J. Siegrist, D. Kinahan, G. Aguirre, G. Kijanka, R. A. Gorkin Iii and J. Ducrée, *Curr. Opin. Chem. Biol.*, 2012, **16**, 409–414.
32 M. Glynn, D. Kirby, D. Chung, D. J. Kinahan, G. Kijanka and J. Ducree, *J. Lab. Autom.*, 2014, **19**, 285–296.
33 M. C. R. Kong and E. D. Salin, *Anal. Chem.*, 2010, **82**, 8039–8041.
34 A. Lee, J. Park, M. Lim, V. Sunkara, S. Y. Kim, G. H. Kim, M. H. Kim and Y. K. Cho, *Anal. Chem.*, 2014, **86**, 11349–11356.
35 O. Strohmeier, M. Keller, F. Schwemmer, S. Zehnle, D. Mark, F. von Stetten, R. Zengerle and N. Paust, *Chem. Soc. Rev.*, 2015, **44**, 6187–6229.
36 M. Tang, G. Wang, S.-K. Kong and H.-P. Ho, *Micromachines*, 2016, **7**, 1–29.
37 J. Zhang, N. Chintalaramulu, R. Vadivelu, H. An, D. Yuan, J. Jin, C. H. Ooi, I. E. Cock, W. Li and N.-T. Nguyen, *Anal. Chem.*, 2020, **92**, 11558–11564.
38 T. S. H. Tran, B. D. Ho, J. P. Beech and J. O. Tegenfeldt, *Lab Chip*, 2017, **17**, 3592–3600.
39 Z. Wu, Y. Chen, M. Wang and A. J. Chung, *Lab Chip*, 2016, **16**, 532–542.
40 A. Sarkar, H. W. Hou, A. E. Mahan, J. Han and G. Alter, *Sci. Rep.*, 2016, **6**, 23589.
41 J. Zhou, P. V. Giridhar, S. Kasper and I. Papautsky, *Lab Chip*, 2013, **13**, 1919–1929.
42 J. Zhou, P. V. Giridhar, S. Kasper and I. Papautsky, *Biomicrofluidics*, 2014, **8**, 044112.
43 H. Amini, W. Lee and D. Di Carlo, *Lab Chip*, 2014, **14**, 2739–2761.
44 J. M. Martel and M. Toner, *Annu. Rev. Biomed. Eng.*, 2014, **16**, 371–396.
45 J. Zhang, S. Yan, D. Yuan, G. Alici, N.-T. Nguyen, M. E. Warkiani and W. Li, *Lab Chip*, 2016, **16**, 10–34.
46 A. Mashhadian and A. Shamloo, *Anal. Chim. Acta*, 2019, **1083**, 137–149.
47 Y. Ying and Y. Lin, *Sci. Rep.*, 2019, **9**, 1–12.
48 M. Rafeie, S. Hosseinzadeh, R. A. Taylor and M. E. Warkiani, *Biomicrofluidics*, 2019, **13**, 034117.
49 Y. Gou, S. Zhang, C. Sun, P. Wang, Z. You, Y. Yalikun, Y. Tanaka and D. Ren, *Anal. Chem.*, 2019, **92**, 1833–1841.
50 N. Xiang, Q. Li and Z. Ni, *Anal. Chem.*, 2020, **92**, 6770–6776.
51 X. Lu, J. J. M. Chow, S. H. Koo, T. Y. Tan, B. Jiang and Y. Ai, *Anal. Chem.*, 2020, **92**, 15579–15586.
52 E. Ozkumur, A. M. Shah, J. C. Ciciliano, B. L. Emmink, D. T. Miyamoto, E. Brachtel, M. Yu, P.-I. Chen, B. Morgan and J. Trautwein, *Sci. Transl. Med.*, 2013, **5**, 179ra147–179ra147.
53 H. Cha, H. Fallahi, Y. Dai, S. Yadav, S. Hettiarachchi, A. McNamee, H. An, N. Xiang, N.-T. Nguyen and J. Zhang, *Lab Chip*, 2022, **22**, 2789–2800.
54 J. Zhou and I. Papautsky, *Lab Chip*, 2013, **13**, 1121–1132.
55 C. Renier, E. Pao, J. Che, H. E. Liu, C. A. Lemaire, M. Matsumoto, M. Triboulet, S. Srivinas, S. S. Jeffrey and M. Rettig, *npj Precis. Oncol.*, 2017, **1**, 1–11.
56 Z. Wu, Y. Chen, M. Wang and A. J. Chung, *Lab Chip*, 2016, **16**, 532–542.
57 J. Cruz, T. Graells, M. Walldén and K. Hjort, *Lab Chip*, 2019, **19**, 1257–1266.

58 M. Masaeli, E. Sollier, H. Amini, W. Mao, K. Camacho, N. Doshi, S. Mitragotri, A. Alexeev and D. Di Carlo, *Phys. Rev. X*, 2012, **2**, 031017.
59 S. C. Hur, S.-E. Choi, S. Kwon and D. D. Carlo, *Appl. Phys. Lett.*, 2011, **99**, 044101.
60 N.-T. Nguyen, S. T. Wereley and S. A. M. Shaegh, *Fundamentals and applications of microfluidics*, Artech house, 2019.
61 X. Li, Y. Zhou, B. Wickramaratne, Y. Yang and D. Pappas, *Biomed. Microdevices*, 2021, **23**, 1–10.
62 R. Khojah, R. Stoutamore and D. Di Carlo, *Lab Chip*, 2017, **17**, 2542–2549.
63 X. Li, Y. Zhou, B. Wickramaratne, Y. Yang and D. Pappas, *Biomed. Microdevices*, 2021, **23**, 28.
64 B. Wickramaratne and D. Pappas, *RSC Adv.*, 2020, **10**, 32628–32637.

Published on 08 September 2022. Downloaded on 1/27/2026 6:45:06 AM.


This journal is © The Royal Society of Chemistry 2022